https://doi.org/10.31891/2307-5732-2026-361-3
УДК 004.8:528.8:621.396.96

АЛЬ-СЕНАЙХ РАЕД
Національний аерокосмічний університет «ХАІ», Харків, Україна
https://orcid.org/0000-0002-8059-4237
e-mail: r.z.alsenaikh@khai.edu
РУБЕЛЬ ОЛЕКСІЙ
Національний аерокосмічний університет «ХАІ», Харків, Україна
https://orcid.org/0000-0001-6206-3988
e-mail: rubel@khai.edu

ПРОГНОЗУВАННЯ ОПТИМАЛЬНОГО РОЗМІРУ ВІКНА ФІЛЬТРА LEE ДЛЯ PCA-ЗОБРАЖЕНЬ SENTINEL-1 З ВИКОРИСТАННЯМ ТРАНСФЕРНОГО НАВЧАННЯ НА MOBILENETV2

В роботі запропоновано метод апріорного вибору оптимального розміру вікна фільтра Lee для придушення спекл-шуму в PCA-зображеннях Sentinel-1 на основі трансферного навчання з MobileNetV2. Навчання проведено на синтетичних даних з ENL [2;6]; отримано точність класифікації до 87,17% (FSIM) і збалансовану точність 88,94% (MS-SSIM). Метод стійкий до варіацій шуму та придатний для автоматизованих конвеєрів обробки PCA-даних без апріорного знання ENL.

Ключові слова: *спекл-шум; Sentinel-1; фільтр Lee; вибір розміру вікна; MobileNetV2; трансферне навчання.*

AL-SENAIKH RAED, RUBEL OLEKSII
National Aerospace University «Kharkiv Aviation Institute», Kharkiv, Ukraine

PREDICTING OPTIMAL LEE FILTER WINDOW SIZE FOR SENTINEL-1 SAR IMAGES USING TRANSFER LEARNING ON MOBILENETV2

A method for a priori selection of the optimal Lee filter window size for speckle noise suppression in Sentinel-1 SAR images is presented. The task is formulated as a direct multiclass classification problem. The proposed model employs transfer learning with a compact MobileNetV2 backbone adapted to single-channel SAR input and equipped with a lightweight classification head. The training corpus is generated synthetically: Sentinel-2 images are aligned to the Sentinel-1 distribution via histogram matching and subjected to dynamic multiplicative noise with gamma distribution and controlled spatial correlation. Ground truth labels are determined by exhaustive Lee filtering with window sizes of 3×3, 5×5, 7×7, 9×9, and 11×11, selecting argmax over the full quality metric. Six independent experiments were conducted for PSNR, SSIM, MS-SSIM, FSIM, HaarPSI, and MDSI criteria. On a test set of 382 images (1024×1024), the best overall accuracy reached 87.17% (FSIM), balanced accuracy achieved 88.94% (MS-SSIM), minimum calibration error ECE was 0.0371 (PSNR), Brier score was 0.0359 (FSIM), with Top-2 accuracy in the range of 99.21–100.00% (100.00% for PSNR). Across ENL bins, accuracy remained ≥ 80% and reached 91.1% for [2.0, 3.0) with PSNR and FSIM; across speckle spatial frequency scale, peaks of 93.7% (FSIM) at [0.72, 0.86) and 93.0% (MS-SSIM) at [0.58, 0.72) were observed. Critically, the method does not require a priori knowledge of the equivalent number of looks (ENL), which is consistent with accuracy stability in the range [2.0, 6.0]. The method is suitable for operational integration into production SAR pipelines for preprocessing and computational resource planning.

Keywords: *Speckle noise; Sentinel-1; Lee filter; window-size selection; MobileNetV2; transfer learning*

Стаття надійшла до редакції / Received 12.11.2025
Прийнята до друку / Accepted 11.01.2026
Опубліковано / Published 29.01.2026

Introduction

The Lee filter is one of the most widely used adaptive filters for speckle noise suppression in SAR images [1, 2]. However, filtering efficiency critically depends on the choice of filter window size, which determines the balance between noise suppression and preservation of structural image details. A window that is too small may insufficiently suppress noise, whereas an excessively large window may lead to blurring of important details and edges [3, 4].

The selection of optimal window size is traditionally performed empirically or through exhaustive search over all possible values, which requires substantial computational resources and is unsuitable for automated SAR data processing systems. A priori prediction of the optimal window size would significantly reduce processing time and enhance the efficiency of automated pipelines.

The objective of this work is to develop a method for a priori prediction of the optimal Lee filter window size for noisy Sentinel-1 SAR images using deep learning.

The novelty lies in formulating the filter parameter selection task as a direct classification problem using transfer learning. Unlike existing approaches based on regression prediction of quality metrics followed by maximum selection [5] or on statistical features and heuristic rules, the proposed method automatically extracts relevant features from images and directly predicts the optimal window size as a class, eliminating the need for a two-stage process (regression + argmax) and ensuring higher operational efficiency.

The following notation is adopted throughout the paper: S1-SAR denotes Sentinel-1 images in Interferometric Wide swath Ground Range Detected (IW GRD) mode with vertical-vertical (VV) polarization, as provided by the Sentinel-1 satellite; S2-NIR denotes Sentinel-2 optical images at Level 2A (L2A) processing level, Band 8 (B8, near-infrared, 10 m spatial resolution), as provided by the Sentinel-2 satellite. All derived versions (after p98-clipped max normalization, histogram matching, speckle addition/filtering) are designated with the same prefixes.

Related Work

Speckle noise suppression is a critically important task in synthetic aperture radar (SAR) image processing [1, 2]. Speckle noise, arising from coherent scattering, hinders visual interpretation and automated analysis of SAR data, including classification and segmentation [3]. The Lee filter [4] is one of the most widely used and effective local statistical filters for speckle reduction, but its performance substantially depends on the correct selection of the scanning window size.

Traditional approaches to Lee filter window size selection are often based on empirical rules or require iterative procedures. Optimization methods such as Grid Search, Random Search, and Bayesian Optimization [6], while capable of finding optimal parameters, are unsuitable for operational use due to high computational complexity, as they require multiple filter applications for each image. This creates a significant barrier to real-time adaptive filtering applications.

In recent years, approaches to a priori prediction of filtering efficiency using machine learning methods have been actively developed. These studies aim to reduce computational costs by predicting optimal parameters or filtering quality without exhaustive search. Specifically, [5] demonstrated the feasibility of global Lee filter window size selection based on predicting quality metric increments (PSNR, PSNR-HVS-M, FSIM) using a trained neural network. That work showed that the probability of correct window selection for five classes (3×3, 5×5, 7×7, 9×9, 11×11) can reach 0.86–0.92, with substantial metric gains relative to "average" choices. The authors also identified robust patterns: large windows are preferable in homogeneous regions with strong speckle, whereas small windows better preserve edges and textures in complex scenes. These results support the formulation of a priori classification of optimal window size and provide the basis for selecting target metrics and class ranges in our work.

Complementary studies address automated threshold selection in alternative despeckling pipelines, such as the DCT-SSA filter [7], where various decision strategies were benchmarked to balance speckle suppression against structural fidelity—further underscoring the need for direct parameter prediction mechanisms in operational SAR workflows.

However, existing approaches predominantly focus on regression models for quality metric prediction, which require a subsequent decision-making step for optimal parameter selection. This limits their operational efficiency and applicability in scenarios requiring rapid, a priori selection of filtering parameters. Thus, there exists a clear research gap in developing methods that directly address the classification task of optimal Lee filter window size for SAR images, leveraging modern deep neural network architectures with emphasis on computational efficiency. The present work aims to fill this gap by proposing an approach that fundamentally differs from previous research focused on resource-intensive parametric search or regression prediction, while ensuring high operational efficiency and solution accuracy.

Methodology

The developed methodology integrates a lightweight convolutional architecture for classifying Lee filter window sizes with a dedicated ground-truth label generation pipeline based on exhaustive search over candidate parameters. The proposed model employs the MobileNetV2 network [8], pretrained on the ImageNet dataset, as its backbone. This architecture was selected for its computational efficiency when processing large images: it provides substantial reduction in video memory consumption (up to 60% compared to DenseNet-121) while maintaining sufficient expressive capacity for the parameter classification task. To adapt the network to single-channel SAR images, several architectural modifications were implemented:

- the input Conv2d layer was modified from format (3, 32, 3 × 3) to (1, 32, 3 × 3) with weight averaging across channels;
- the classification head was replaced with a Linear(1280, 5) layer followed by Softmax for classification of five window sizes;
- the original inverted residual blocks structure was preserved for efficient feature extraction.

A full fine-tuning strategy is employed, in which all network layers are trained jointly. The loss function is CrossEntropyLoss with class weights for balancing [9, 10].

Adaptive average pooling to a fixed spatial size is applied to match feature space dimensions, ensuring invariance to input resolution and preservation of aggregated spatial-textural information characteristic of speckle structures. A compact classification head is used atop the network body: $\mathrm{Dropout}(0.3) \to \mathrm{Linear}(\cdot, 512) \to \mathrm{ReLU} \to \mathrm{Dropout}(0.2) \to \mathrm{Linear}(512,5)$. This configuration reduces overfitting risk, stabilizes posterior class probability estimation, and enhances sensitivity to local and medium-scale textural patterns critical for optimal Lee filter window size selection.

The synthetic data generation pipeline employs histogram matching of Sentinel-2 optical images to Sentinel-1 SAR references and dynamic speckle noise addition with ENL ∈ [2, 6] (as detailed in [11]).

The dynamic speckle noise overlay module implements physically consistent observation formation in the intensity domain. The stylized image I_{style} (amplitude representation) is first converted to the intensity domain (squaring). Then, multiplicative noise S with gamma distribution S ~ Γ(L, 1/L) is applied to the intensities, where L is interpreted as the equivalent number of looks (ENL) and is sampled from the interval $[L_{\min}, L_{\max}]$ for each iteration. After noise application, inverse transformation to the amplitude domain and joint normalization of the result with the original image by a single coefficient are performed, eliminating scale shifts and ensuring comparable dynamic ranges when computing quality metrics.

To model diverse spatial correlation of speckle grains, an additional parameter $s \in [s_{\min}, s_{\max}]$ is introduced — the speckle spatial frequency scale, inversely proportional to the characteristic speckle grain size λ_{noise}: $\lambda_{\text{noise}} \propto 1/s$. The parameter s specifies the internal resolution of the noise field before resampling. Let I denote the scene amplitude and S the intensity noise with E[S] = 1. Then, the formation of noisy amplitude and sampling parameters is given by

$$\tilde{I} = \sqrt[2]{(I^2) \cdot S}, \quad S \sim \Gamma(L, 1/L), \quad L \sim \mathcal{U}(L_{\min}, L_{\max}), \quad s \sim \mathcal{U}(s_{\min}, s_{\max}). \tag{1}$$

Subsequently, joint normalization by maximum is performed:

$$\alpha = \left(\max_{c,h,w} \tilde{I}_{c,h,w}\right)^{-1}, \quad I_{\text{noisy}} = \alpha \tilde{I}, \quad I_{\text{reference}} = \alpha I, \tag{2}$$

which ensures comparability of dynamic ranges, improves numerical stability of computations, and stabilizes the training process.

The process of ground-truth label formation and model training is implemented as follows. The dynamic speckle noise overlay module generates a noisy image I_{noisy} and corresponding reference image $I_{\text{reference}}$. The noisy image I_{noisy} is fed to the trained model to obtain a prediction ŷ of the optimal filter window size within the classification task framework. In parallel, I_{noisy} is converted to intensities, filtered by the Lee algorithm for w ∈ {3, 5, 7, 9, 11}, and converted back to amplitudes: $I_{\text{filtered},w} = \sqrt{\text{LeeFilter}\left(I_{\text{noisy}}^2, w\right)}$. Operations are performed in the intensity domain, as in the standard Lee filter implementation for SAR. For each filtered image $I_{\text{filtered},w}$, a quality metric is computed by comparison with the reference image $I_{\text{reference}}$: $M_w = \text{Metric}(I_{\text{filtered},w}, I_{\text{reference}})$, where Metric ∈ {PSNR, SSIM, MS-SSIM, FSIM, HaarPSI, MDSI}. The use of visual quality metrics for assessing filtering efficiency in SAR images is well-established in the literature [12, 13, 14], as these metrics effectively capture perceptual differences and structural characteristics that are critical for evaluating speckle noise suppression while preserving image details.

PSNR (Peak Signal-to-Noise Ratio) [15].

$$\text{PSNR}_w = 20\log_{10}\left(\frac{\text{MAX}_I}{\sqrt[2]{\text{MSE}_w}}\right), \quad \text{MSE}_w = \frac{1}{HW}\sum(I_{\text{filtered},w} - I_{\text{reference}})^2, \tag{3}$$

where MSE_w is the mean squared error between filtered and reference images, MAX_I is the maximum intensity value, H and W are image height and width.

SSIM (Structural Similarity Index) [15].

$$\text{SSIM}_w(x,y) = \frac{(2\mu_x\mu_y + C_1)(2\sigma_{xy} + C_2)}{(\mu_x^2 + \mu_y^2 + C_1)(\sigma_x^2 + \sigma_y^2 + C_2)}, \tag{4}$$

where μ_x, μ_y are mean brightness values of images x = $I_{\text{filtered},w}$ and y = $I_{\text{reference}}$, σ_x^2, σ_y^2 are variances (contrast), σ_{xy} is the covariance between images (structure), and $C_1 = 0.01^2, C_2 = 0.03^2$ are stabilization constants.

MS-SSIM (Multi-Scale Structural Similarity Index) [15].

$$\text{MS-SSIM}_w(x,y) = \prod_{j=0}^{4}\left[\text{SSIM}(x_j, y_j)\right]^{w_j}, \tag{5}$$

where x_j, y_j are images at scale j after downsampling, w_j are weighting coefficients ($w_0 = 0.0448, w_1 = 0.2856, w_2 = 0.3001, w_3 = 0.2363, w_4 = 0.1333$).

FSIM (Feature Similarity Index) [16].

$$\text{FSIM}_w = \frac{\sum_{p\in\Omega} S_{PC}(p) S_G(p)}{\sum_{p\in\Omega} S_G(p)}, \tag{6}$$

where $S_{PC}(p)$ is phase congruency at point p, $S_G(p)$ is gradient similarity, Ω is the set of all image pixels.

HaarPSI (Haar Perceptual Similarity Index) [17].

$$\text{HaarPSI}_w = 1 - \frac{\sum_k \alpha_k d_k}{\sum_k \alpha_k}, \tag{7}$$

where d_k is the Haar distance at decomposition level k, α_k are weights corresponding to the importance of different frequency bands in the wavelet decomposition.

MDSI (Mean Deviation Similarity Index) [18].

$$\text{MDSI}_w = 1 - \frac{1}{|\Omega|}\sum_{p\in\Omega}\left[\beta_1 D_g(p) + \beta_2 D_c(p) + \beta_3 D_s(p)\right], \tag{8}$$

where $D_g(p)$ is the gradient difference, $D_c(p)$ is the contrast difference, $D_s(p)$ is the structural difference, and $\beta_1, \beta_2, \beta_3$ are weighting coefficients.

The selection of these six quality metrics is motivated by their complementary coverage of image quality aspects. PSNR (3) provides a pixel-level error baseline; SSIM (4) and MS-SSIM (5) capture structural similarity at single and multiple scales; FSIM (6) assesses local feature preservation via phase congruency and gradients. HaarPSI (7), built on Haar wavelet decomposition, measures perceptual similarity across spatial frequency bands and naturally reflects the multi-scale character of speckle and SAR textures, enabling evaluation of how window sizes preserve or attenuate features at different spatial frequencies [12, 13, 14]. MDSI (8) jointly evaluates gradient-, contrast-, and structure-related differences, which aligns with the multiplicative nature of speckle that perturbs both local contrast and global structure; this makes MDSI effective for quantifying the noise–detail trade-off under Lee filtering in SAR imagery [12, 13, 14]. This mix of traditional (PSNR, SSIM) and perceptual (FSIM, HaarPSI, MDSI) metrics ensures robust evaluation across complementary quality criteria.

The optimal window size is determined as $y = \text{argmax}_w M_w$ and used as the ground-truth label. The loss function is weighted cross-entropy over the true class: $L = -w_y \log(\hat{p}_y)$, $\hat{p}_i = \frac{\exp z_i}{\sum_{j=1}^{5}\exp z_j}$, $y \in \{1, \ldots, 5\}$, where z_i are

model logits, $\hat{p}_i$ are softmax probabilities, w_y is the true class weight for balancing imbalanced data [9, 10]. Equivalent notation via indicator: $L = -\sum_{i=1}^{5} w_i \mathbb{1}[i = y] \log(\hat{p}_i)$.

Class weights are determined by inverting class frequency in the training set (for the specific quality metric) and normalized by the number of classes: $w_i = \frac{N}{Kn_i}$, where K = 5, $N = \sum_{j=1}^{K} n_j$, and n_i is the number of samples of class i in the training subset of the current experiment. This definition reduces the influence of prevalent classes and stabilizes training under class imbalance.

The Lee filter implementation operates in the intensity domain: local means and variances are estimated over window w × w, while noise variance is approximated via the squared global coefficient of variation of intensity (consistent with the assumption $\sigma_n^2 \approx 1/L$ for unknown L). Weights are computed by the classical Lee formula $w = \frac{\sigma^2_{\text{local}}}{\sigma^2_{\text{local}} + \sigma_n^2 \mu^2_{\text{local}}}$ with numerically stable constraints on minimum variance. For the MDSI metric, which is a distance measure, the optimum is selected via $\text{argmin}_w M_w$, whereas for other metrics $\text{argmax}_w M_w$ is used.

The work investigates the influence of quality metric choice on the accuracy of predicting optimal filter parameters. For each quality metric (PSNR, SSIM, MS-SSIM, FSIM, HaarPSI, MDSI), a separate experiment is conducted, including ground-truth label formation, model training, and testing, since ground-truth labels are determined based on the selected metric. Thus, six independent experiments were conducted, one for each quality metric.

To assess the robustness of the method to variations in noise parameters, stratified analysis is performed across ENL (equivalent number of looks) bins and speckle spatial frequency scale. The analysis includes computation of classification accuracy and optimal class distributions for different parameter ranges, enabling identification of dependencies between noise characteristics and optimal filter window size.

Experimental Setup

The synthetic dataset (1910 S2-NIR images stylized to the S1-SAR radiometric distribution via histogram matching with references) was split 80/20 into training (1528 images) and test (382 images) subsets. The distribution of optimal window sizes in the test set for the PSNR metric: 3×3 — 67 images (17.5%), 5×5 — 421 images (26.0%), 7×7 — 530 images (34.7%), 9×9 — 309 images (20.3%), 11×11 — 201 images (13.2%). This example is for PSNR; the other metrics (SSIM, MS-SSIM, FSIM, HaarPSI, MDSI) are analyzed equivalently. The class distribution is imbalanced, which is accounted for when computing class weights and when evaluating the balanced accuracy metric.

For each quality metric, separate model training is conducted, since ground-truth labels are formed based on the selected metric. Six experiments were performed in total: one for each of the investigated quality metrics (PSNR, SSIM, MS-SSIM, FSIM, HaarPSI, MDSI). Before each experiment (before training with a specific quality metric), class weights w_i are computed once for balancing imbalanced data based on the class distribution in the training set for that metric. Class weights are determined separately for each experiment, since the distribution of optimal window sizes may differ depending on the selected quality metric used for forming ground-truth labels. Models were trained in PyTorch using an NVIDIA RTX 4090 GPU. With the MobileNetV2 architecture, batch size was set to 8 images. Training hyperparameters are identical for all experiments. Training was conducted using the Adam optimizer with learning rate $\eta = 10^{-4}$ for 60 epochs. Batch size was 8 images of size 1024 × 1024 pixels. CrossEntropyLoss with class weights for balancing imbalanced data [9, 10] was used as the loss function. Due to the efficiency of the MobileNetV2 architecture, gradient accumulation was not required; gradients were updated at each training step.

Classification performance is evaluated using a comprehensive set of metrics that capture different aspects of model accuracy, calibration quality, and robustness to class imbalance. The following notation is adopted throughout this section: N denotes the total number of examples, C is the number of classes, TP_i, FP_i, and FN_i represent the counts of true positive, false positive, and false negative predictions for class i, respectively. Elements of the confusion matrix are denoted as CM_{ij}, where i indicates the true class and j the predicted class. For top-k accuracy evaluation, TopK_n denotes the set of k most probable predictions for example n, and y_n represents the true label. In calibration analysis, B denotes the number of calibration bins, n_b is the number of examples in bin b, while $\text{acc}(b)$ and $\text{conf}(b)$ represent the actual accuracy and average confidence in bin b, respectively.

Overall Accuracy measures the fraction of correctly classified examples across all classes. Given the imbalanced nature of the classification task, this metric provides a baseline assessment but may be biased toward majority classes. The accuracy is computed as

$$\text{Accuracy} = \frac{\text{TP}_{\text{total}}}{N} = \frac{\sum_{i=1}^{C} \text{TP}_i}{N}. \quad (9)$$

Balanced Accuracy addresses class imbalance by computing the average per-class sensitivity, providing equal weight to each class regardless of its frequency. This metric is particularly relevant for evaluating performance on imbalanced datasets and is defined as

$$\text{Balanced Accuracy} = \frac{1}{C} \sum_{i=1}^{C} \frac{\text{TP}_i}{\text{TP}_i + \text{FN}_i}. \quad (10)$$

Recall for class i quantifies the fraction of correctly identified objects belonging to class i, measuring the model's ability to detect instances of each class. The per-class recall is given by

$$\text{Recall}_i = \frac{\text{TP}_i}{\text{TP}_i + \text{FN}_i}. \quad (11)$$

Top-k Accuracy evaluates the model's performance when considering the k most probable predictions, which is particularly useful for assessing the robustness of classification decisions. This metric measures the fraction of examples for which the true class is among the k most probable model predictions. For the general case, Top-k Accuracy is defined as

$$\text{Top-}k\text{Accuracy} = \frac{1}{N}\sum_{n=1}^{N} \mathbb{1}[y_n \in \text{TopK}_n], k \in \{2,3\}. \quad (12)$$

Cohen's Kappa measures the agreement between predictions and true labels while accounting for chance agreement, providing a normalized assessment of classification performance. The Kappa coefficient is computed as $\kappa = \frac{p_o - p_e}{1-p_e}$, where

$$p_o = \frac{1}{N}\sum_{i=1}^{C} CM_{ii}, p_e = \frac{1}{N^2}\sum_{i=1}^{C}\left(\sum_{j=1}^{C} CM_{ij}\right)\left(\sum_{j=1}^{C} CM_{ji}\right), \quad (13)$$

where p_o represents the observed agreement and p_e the expected agreement under chance. Matthews Correlation Coefficient (MCC) extends the binary classification correlation metric to the multiclass case, providing a balanced measure that accounts for all elements of the confusion matrix. The MCC is computed as

$$\text{MCC} = \frac{cs - \sum_{k=1}^{C} p_k t_k}{\sqrt{(s^2 - \sum_{k=1}^{C} p_k^2)(s^2 - \sum_{k=1}^{C} t_k^2)}}, \quad (14)$$

where $c = \sum_{k=1}^{C} CM_{kk}$, $s = \sum_{i=1}^{C}\sum_{j=1}^{C} CM_{ij}$, $p_k = \sum_{i=1}^{C} CM_{ik}$ represents the number of examples predicted as class k, and $t_k = \sum_{j=1}^{C} CM_{kj}$ represents the number of examples with true class k.

Expected Calibration Error (ECE) quantifies the calibration quality of probabilistic predictions by measuring the average absolute discrepancy between accuracy and confidence across calibration bins. Lower ECE values indicate better calibration, meaning that the model's confidence estimates are more reliable. The ECE is defined as

$$\text{ECE} = \sum_{b=1}^{B} \frac{n_b}{N} |\text{acc}(b) - \text{conf}(b)|. \quad (15)$$

Brier Score measures the mean squared error of probabilistic predictions, providing a comprehensive assessment of both calibration and discrimination quality. Lower Brier scores indicate better probabilistic predictions. The Brier score is computed as

$$\text{Brier} = \frac{1}{N}\sum_{n=1}^{N}\sum_{c=1}^{C}(p_{nc} - y_{nc})^2, \quad (16)$$

where p_{nc} is the predicted probability for class c on example n, and y_{nc} is the binary indicator of the true class. The confusion matrix CM provides a detailed breakdown of classification performance, where CM_{ij} represents the number of images with true class i predicted as class j.

Results

Figure 1 presents the model training curves for all quality metrics, showing the dependence of the loss function on epoch number.

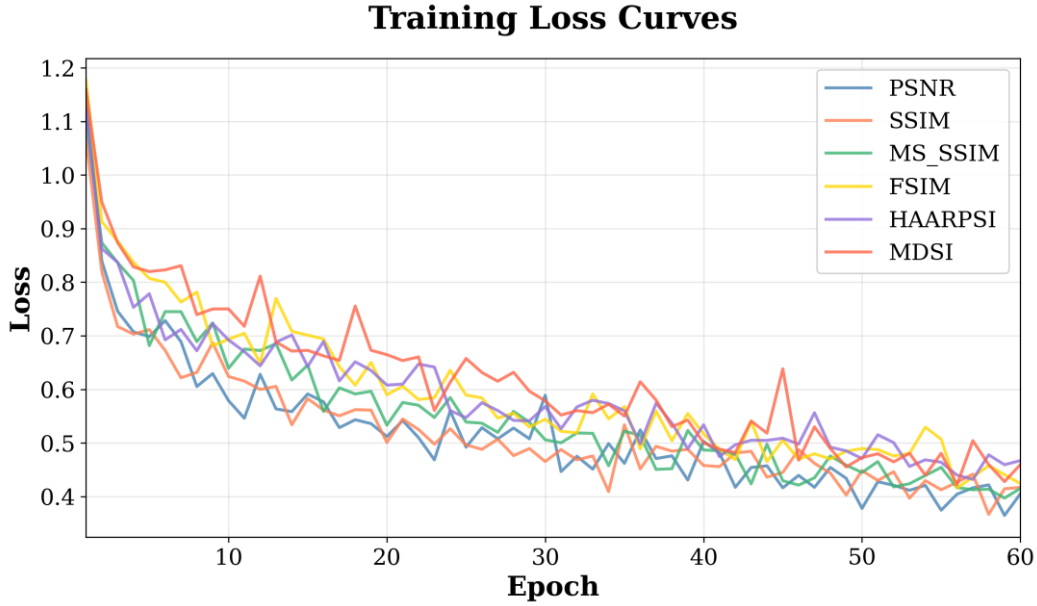

Fig. 1: Model training curves for all quality metrics: dependence of the loss function on the epoch number

Table 1 presents the summary distribution of optimal window sizes across all quality metrics (PSNR, SSIM, MS-SSIM, FSIM, HaarPSI, MDSI). The table shows the percentage ratio and absolute count of images for each window size (3×3, 5×5, 7×7, 9×9, 11×11) for each quality metric.

Table 1

Distribution of optimal window sizes for different quality metrics

Metric	3×3	5×5	7×7	9×9	11×11
PSNR	4.4% (67)	27.6% (421)	34.7% (530)	20.2% (309)	13.2% (201)
SSIM	6.5% (100)	35.3% (540)	32.5% (497)	17.7% (270)	7.9% (121)
MS-SSIM	4.8% (74)	28.2% (431)	30.0% (459)	21.4% (327)	15.5% (237)
FSIM	2.9% (45)	21.3% (325)	29.1% (445)	23.1% (353)	23.6% (360)
HaarPSI	2.5% (38)	21.3% (326)	34.0% (520)	25.0% (382)	17.1% (262)
MDSI	2.4% (36)	15.9% (243)	27.4% (418)	28.1% (429)	26.3% (402)

Table 2 presents the per-class Recall values for all quality metrics. The table shows Recall for each window size (3×3, 5×5, 7×7, 9×9, 11×11) separately for each quality metric.

Table 2

Per-class Recall comparison for different quality metrics

Metric	3×3	5×5	7×7	9×9	11×11
PSNR	0.933	0.930	0.756	0.844	0.943
SSIM	0.964	0.825	0.773	0.919	0.947
MS-SSIM	1.000	0.736	0.966	0.830	0.915
FSIM	0.923	0.848	0.935	0.833	0.833
HaarPSI	0.833	0.812	0.851	0.839	0.851
MDSI	1.000	0.784	0.827	0.810	0.937

Table 3 presents the aggregated classification quality evaluation metrics for all ground-truth label formation variants (PSNR, SSIM, MS-SSIM, FSIM, HaarPSI, MDSI), including Accuracy, Balanced Accuracy, Cohen's Kappa, MCC, ECE, and Brier Score.

Table 3

Classification metrics comparison for different quality metrics

Ground-truth metric	Accuracy	Balanced Accuracy	Top-2 Accuracy	Kappa	MCC	ECE	Brier
FSIM	87.17%	87.46%	99.48%	0.8291	0.8302	0.0772	0.0359
MS-SSIM	86.13%	88.94%	99.74%	0.8173	0.8228	0.0608	0.0373
PSNR	85.86%	88.14%	100.00%	0.8129	0.8164	0.0371	0.0405
MDSI	85.60%	87.16%	99.48%	0.8104	0.8112	0.0479	0.0407
SSIM	84.55%	88.60%	100.00%	0.7955	0.7992	0.0449	0.0428
HaarPSI	83.77%	83.73%	99.21%	0.7859	0.7869	0.0565	0.0473

Table 4 presents the Recall values for all image quality metrics across each class (Lee filter window size). The table shows the fraction of correctly identified objects for each window size separately for each quality metric.

Table 4

Recall for all metrics by class (window sizes)

Metric	3×3	5×5	7×7	9×9	11×11
PSNR	0.933	0.930	0.756	0.844	0.943
SSIM	0.964	0.825	0.773	0.919	0.947
MS-SSIM	1.000	0.736	0.966	0.830	0.915
FSIM	0.923	0.848	0.935	0.833	0.833
HaarPSI	0.833	0.812	0.851	0.839	0.851
MDSI	1.000	0.784	0.827	0.810	0.937

Figure 2 presents reliability diagrams for all considered image quality metrics. The diagrams show the dependence of actual accuracy on predicted model confidence.

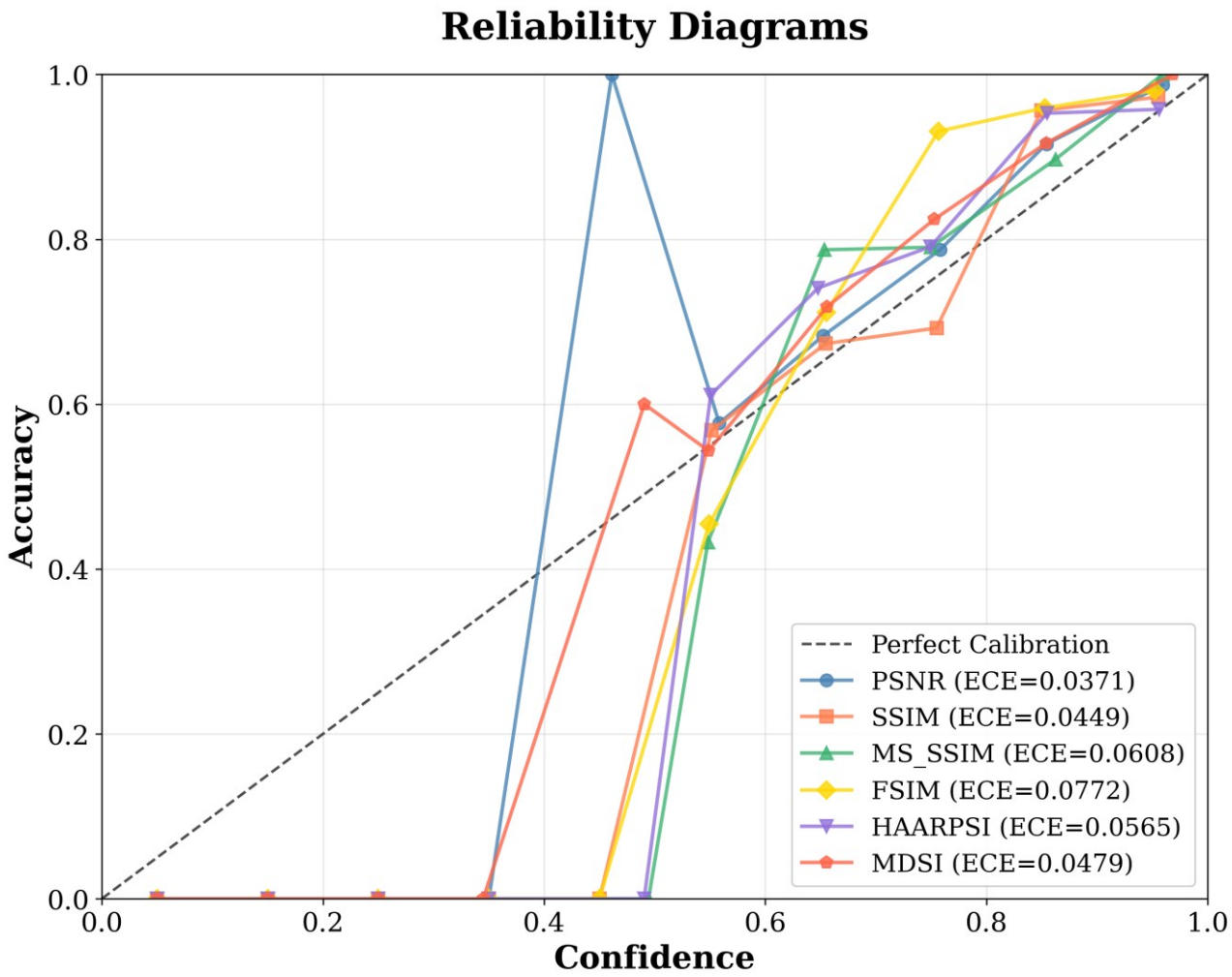

Fig. 2: Reliability diagrams for all metrics: dependence of actual accuracy on predicted model confidence

Table 5 presents the dependence of classification accuracy on ENL (equivalent number of looks) and quality metric. The table shows accuracy values for different ENL ranges ([2.0, 3.0), [3.0, 4.0), [4.0, 5.0), [5.0, 6.0]) separately for each quality metric.

Table 5

Classification accuracy vs. ENL and quality metric

Metric	ENL [2.0, 3.0)	ENL [3.0, 4.0)	ENL [4.0, 5.0)	ENL [5.0, 6.0]
PSNR	91.1%	78.0%	83.2%	90.3%
SSIM	86.5%	85.3%	85.2%	80.7%
MS-SSIM	85.9%	87.2%	83.3%	88.2%
FSIM	91.1%	88.2%	83.8%	86.4%
HaarPSI	86.0%	82.4%	81.2%	86.0%
MDSI	88.9%	90.1%	82.8%	80.2%

Table 6 presents the dependence of classification accuracy on speckle spatial frequency scale and quality metric. The table shows accuracy values for different scale coefficient ranges separately for each quality metric.

Table 6

Classification accuracy vs. spatial frequency scale of speckle and quality metric

Metric	[0.30, 0.44)	[0.44, 0.58)	[0.58, 0.72)	[0.72, 0.86)	[0.86, 1.00]
PSNR	87.4%	84.6%	86.3%	83.8%	87.5%
SSIM	82.9%	88.0%	85.3%	83.1%	83.5%
MS-SSIM	89.2%	85.3%	93.0%	82.1%	82.1%
FSIM	78.2%	84.4%	91.8%	93.7%	87.3%
HaarPSI	84.9%	79.7%	79.4%	88.3%	86.1%
MDSI	90.7%	86.2%	82.9%	82.9%	84.7%

Figure 3 presents the distribution of optimal window sizes across speckle spatial frequency scale for different quality metrics. The plot shows the percentage ratio of each window size (3×3, 5×5, 7×7, 9×9, 11×11) for different scale coefficient ranges separately for each quality metric.

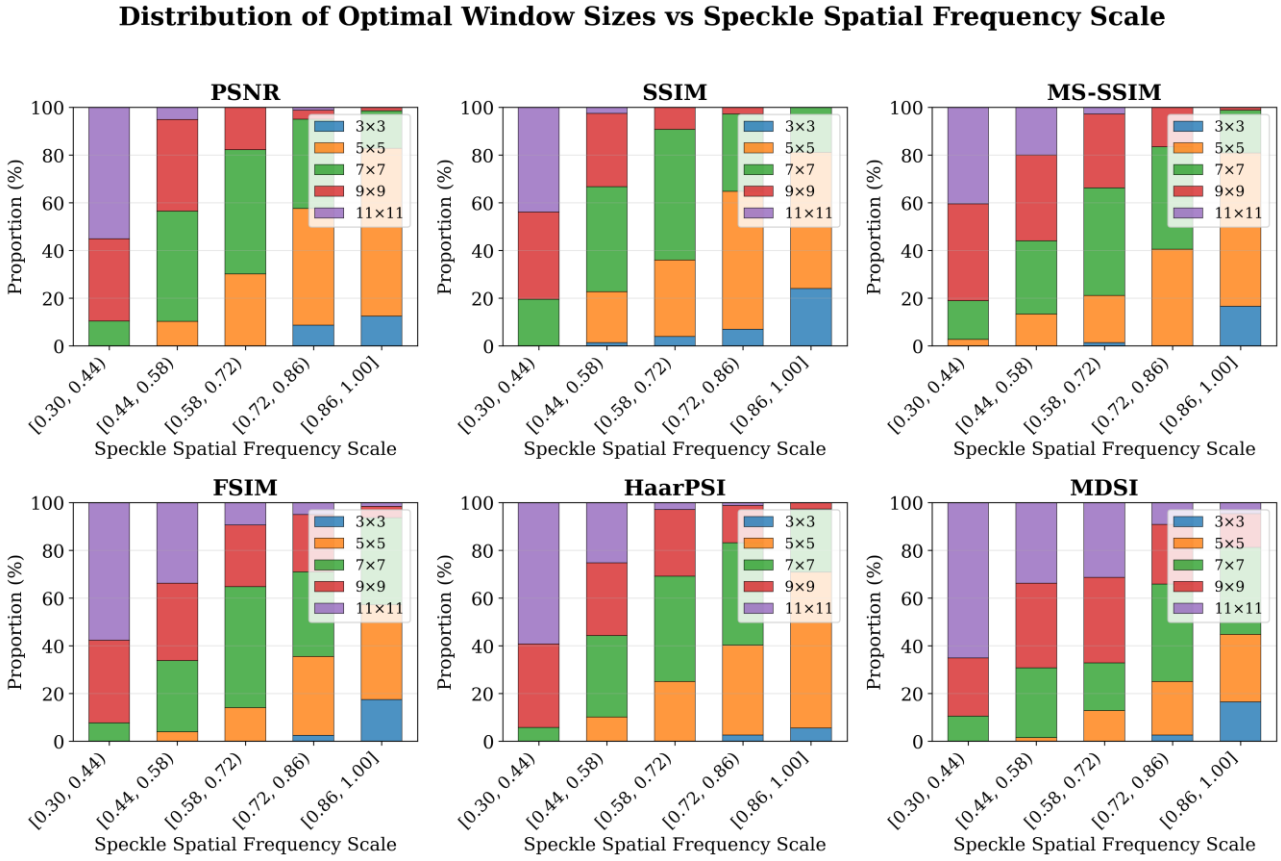

Fig. 3: Distribution of optimal window sizes across speckle spatial frequency scale for different quality metrics

For objective assessment of the predictive efficiency of the proposed approach, a comparison was conducted with the state-of-the-art method [5], where the Lee filter window size selection task is solved via regression prediction of quality metrics followed by argmax. In contrast to the two-stage logic of regression metric prediction (IPSNR, IPHVSM, IFSIM) followed by maximum selection, the proposed method implements direct one-stage classification, eliminating error accumulation at the argmax stage. Architecturally, instead of an MLP on 13 handcrafted statistical features (DCT coefficients, 8×8 block statistics, probabilistic parameters), an adapted MobileNetV2 with transfer learning from ImageNet is used, providing automatic extraction of multilevel textural features from full images of size 1024×1024 pixels versus 512×512 in [5]. Training is conducted on a synthetic corpus with a wide range of noise parameters — random ENL ∈ [2.0,6.0] and speckle spatial frequency scale $s \in [0.3,1.0]$ (uniform distribution for each image) versus fixed ENL ≈ 5 in [5], ensuring method applicability to various Sentinel-1 acquisition conditions. Moreover, analysis across six quality metrics (PSNR, SSIM, MS-SSIM, FSIM, HaarPSI, MDSI) versus three in [5] was conducted, demonstrating comparable window selection accuracy — 85.86% Accuracy (PSNR) versus ~90% in the self-validation scenario [5] — with assessment of probability calibration (ECE=0.0371, Brier=0.0405) and Top-2 Accuracy 100%, unavailable in the regression formulation. Thus, the proposed approach offers an alternative strategy for a priori despeckling parameter selection with emphasis on versatility and one-stage prediction.

Discussion

The distributions in Table 1 reflect the general tradeoff of the Lee filter between speckle noise suppression and detail preservation: increasing window size $w \times w$ reduces variability in local statistics estimates and enhances smoothing, but increases the risk of blurring boundaries and fine structures [4]. For metrics oriented toward pixel-intensity and structural relationships (PSNR, SSIM, MS-SSIM), medium windows (5×5, 7×7) dominate, indicating a balance between noise suppression and structure preservation. For perceptually-oriented metrics (FSIM, HaarPSI), distributions shift toward larger windows (9×9, 11×11) due to greater robustness to small-scale artifacts under moderate smoothing. For the distance metric MDSI, the largest fraction of large windows (9×9, 11×11) is characteristic, consistent with its sensitivity to local distortions in contrast and structure. Collectively, the distributions are consistent with the theoretical foundations of Lee filtering [4] and with typical noise parameter ranges ENL ∈ [2,6] for Sentinel-1 IW GRD images [19], under which medium and large windows are preferable depending on evaluation criteria [6].

Analysis of Tables 2 and 3 shows that overall accuracy reached 85.86%, balanced accuracy — 88.14%. Top-2 accuracy reached 100%, Top-3 accuracy also equals 100%, indicating that the model rarely makes significant errors

in window size selection and the true class is almost always among the three most probable predictions. Low ECE values in Table 3 indicate satisfactory probability calibration of the model, which is also confirmed by the reliability diagrams in Figure 2.

Analysis of Table 5 demonstrates the method's robustness to ENL parameter variations: classification accuracy remains high (above 80%) for all investigated ENL ranges and quality metrics. The highest accuracy is observed for PSNR and FSIM metrics in ENL ranges [2.0,3.0) and [5.0,6.0] (91.1%), indicating method effectiveness for various speckle noise levels characteristic of Sentinel-1 IW GRD images.

Analysis of the distribution of optimal window sizes across speckle spatial frequency scale for different quality metrics (Fig. 3) demonstrates a direct dependence of optimal window size on parameter s, which determines the spatial structure of speckle noise. The observed patterns are consistent across different quality metrics, confirming the robustness of the identified dependencies. According to the methodology (see formula (1) for speckle noise formation), the speckle spatial frequency scale $s \in [s_{\min}, s_{\max}]$ specifies the internal resolution of the noise field before resampling, controlling the spatial scale of correlations in the noise field. At small values of s (e.g., s ∈ [0.3, 0.54)), noise is generated at reduced resolution and then upscaled, creating coarse-scale texture with spatial correlations on scales exceeding the size of small windows. In this case, large windows (9×9, 11×11) are required for effective suppression, confirmed by the prevalence of these classes in the range s ∈ [0.3, 0.54): the fraction of window 11×11 is ~55%, and window 9×9 — ~35%.

The mathematical justification for the relationship between noise scale and Lee filter window size is based on formula (17) for filtering weights, provided in the methodology section:

$$w_{ij} = \frac{\sigma^2_{\text{local}}}{\sigma^2_{\text{local}} + \sigma_n^2 \mu^2_{\text{local}}} \tag{17}$$

where σ^2_{local} is the local intensity variance estimated over window size w × w, $\sigma_n^2 \approx 1/L$ is the noise variance, μ_{local} is the local mean. For effective suppression of coarse-scale noise, the window w × w must encompass at least one period of spatial noise correlation. At small s, the characteristic correlation size is $\lambda_{\text{noise}} \propto 1/s$, requiring windows of size $w \geq \lambda_{\text{noise}}$, explaining the prevalence of large windows at s ∈ [0.3, 0.54).

At medium values of speckle spatial frequency scale s ∈ [0.54, 0.78), a more uniform distribution of window sizes is observed with prevalence of medium sizes (7×7, 9×9), where the fraction of window 7×7 reaches ~45–50%. This reflects a transitional regime in which the characteristic noise correlation scale λ_{noise} is comparable to medium window sizes, providing a balance between effective noise suppression (requiring sufficient number of samples $N = w^2$ for stable estimation of σ^2_{local}) and preservation of local image details.

At large values of speckle spatial frequency scale s ∈ [0.78, 1.0], the characteristic noise correlation scale decreases ($\lambda_{\text{noise}} \propto 1/s$), and noise becomes fine-scale. In this range, small windows (3×3, 5×5) provide optimal suppression: the fraction of window 5×5 reaches ~50–70% at s ∈ [0.72, 1.0], and the fraction of window 3×3 increases to ~12% at s ∈ [0.86, 1.0]. Mathematically, this is explained by the fact that for fine-scale noise, large windows $w \gg \lambda_{\text{noise}}$ are excessive and lead to over-smoothing, degrading the PSNR metric due to blurring of edges and local details. Small windows $w \approx \lambda_{\text{noise}}$ provide sufficient samples for local statistics estimation ($N = w^2 \geq 9$ for w ≥ 3) with minimal detail blurring, maximizing PSNR according to formula (3), where MSE_w is minimized at the optimal balance between noise suppression and detail preservation.

To assess the method's robustness to target metric selection, six independent experiments were conducted, each including ground-truth label formation based on the corresponding quality metric, model training, and testing. Results analysis demonstrates that the highest classification accuracy is achieved using FSIM (87.17%) and MS-SSIM (86.13%) for ground-truth label formation. The high effectiveness of FSIM, based on phase congruency and gradients, may be associated with its ability to assess local differences and account for the importance of various image regions, which is critically important for SAR data with their specific textural characteristics [12, 13]. Meanwhile, MS-SSIM demonstrates the highest balanced accuracy (88.94%) and best calibration (ECE = 0.0608), indicating its robustness to class imbalance.

Metrics oriented toward structural similarity (SSIM, MS-SSIM) show high balanced accuracy (88.60% and 88.94% respectively), which may be related to their ability to account for structural image characteristics in the context of multiplicative speckle noise. PSNR demonstrates good overall accuracy (85.86%) and best calibration (ECE = 0.0371), confirming its versatility for SAR image filtering parameter optimization tasks. MDSI shows intermediate results (85.60% accuracy, 87.16% balanced accuracy), which may be related to its ability to account for both structural and contrast differences [18].

It should be noted that HaarPSI demonstrates lower accuracy (83.77%) and balanced accuracy (83.73%), which may be related to specifics of its application to SAR data. Despite the fact that HaarPSI and MDSI were originally developed for optical image quality assessment and may not fully account for specific SAR data characteristics such as multiplicative speckle noise, the obtained results demonstrate their applicability to filtering parameter optimization tasks [12, 14], opening prospects for further research on adapting perceptual quality metrics to SAR image specifics.

Conclusion

A method for a priori selection of the optimal Lee filter window size for speckle noise suppression in Sentinel-1 SAR images is presented, based on transfer learning of an adapted MobileNetV2 architecture. The key distinction from existing approaches lies in formulating the task as direct multiclass classification, eliminating the need for a two-

stage process of quality metric regression prediction followed by maximum selection. On a test set of 382 images (1024×1024), the method demonstrates accuracy up to 87.17% (FSIM) and balanced accuracy up to 88.94% (MS-SSIM) with satisfactory probability calibration (ECE=0.0371 for PSNR) and Top-2 Accuracy 100%. Stratified analysis across ENL and speckle spatial frequency scale confirms the method's robustness to noise parameter variations, ensuring its applicability to various Sentinel-1 acquisition conditions without a priori knowledge of the equivalent number of looks.

This work makes several contributions to the problem of a priori selection of Lee filter parameters for Sentinel-1 SAR despeckling. First, it formulates the filter parameter selection task as a direct multiclass classification problem, thereby eliminating error accumulation at the regression–argmax stage that is characteristic of prior approaches. Second, it adapts the MobileNetV2 architecture with transfer learning for single-channel SAR imagery, enabling efficient extraction of multiscale textural representations under strict memory constraints. Third, it constructs a synthetic training corpus with controlled diversity of noise parameters (ENL $\in [2.0,6.0]$, speckle spatial frequency scale $s \in [0.3,1.0]$) and ground-truth label generation via exhaustive search over six perceptual and signal-based quality metrics. Finally, it provides a systematic evaluation of how the choice of quality metric affects predictive performance and demonstrates empirical robustness of the proposed method to pronounced class imbalance. The proposed approach enables automated a priori selection of despeckling parameters and is readily integrable into operational Sentinel-1 SAR data processing pipelines.

Future research will focus on extending the framework to other despeckling filters and their parameter spaces, jointly optimizing multiple filter parameters within a unified learning setup, and performing comprehensive validation on real Sentinel-1 acquisitions as well as other SAR sensors. Further priorities include incorporating explicit uncertainty quantification for both predicted parameters and quality metrics, investigating alternative target criteria—such as modern perceptual measures including HaarPSI and MDSI—that exhibit improved correlation with subjective quality judgments, and developing models for a priori prediction of quality metric values (HaarPSI, MDSI, SSIM, MS-SSIM, FSIM) for selected filter parameters, thereby enabling estimation of expected despeckling quality before applying the filter.

Acknowledgment

The authors would like to thank the developers of the Copernicus Data Space Ecosystem for providing free access to Sentinel-1 and Sentinel-2 data. This work was supported by the National Aerospace University «KhAI» research facilities.

Література

1. Oliver C. Understanding Synthetic Aperture Radar Images / C. Oliver, S. Quegan. – Raleigh : SciTech Publishing, 2004. – 480 p.
2. Lee J. S. Polarimetric Radar Imaging: From Basics to Applications / J. S. Lee, E. Pottier. – Boca Raton : CRC Press, 2009. – 386 p.
3. Touzi R. A review of speckle filtering in the context of estimation theory / R. Touzi // IEEE Transactions on Geoscience and Remote Sensing. – 2002. – Vol. 40, № 11. – P. 2392–2404. – DOI: https://doi.org/10.1109/TGRS.2002.803727.
4. Lee J. S. Digital image enhancement and noise filtering by use of local statistics / J. S. Lee // IEEE Transactions on Pattern Analysis and Machine Intelligence. – 1980. – Vol. 2, № 2. – P. 165–168. – DOI: https://doi.org/10.1109/TPAMI.1980.4766994.
5. Rubel O. Selection of Lee filter window size based on despeckling efficiency prediction for Sentinel SAR images / O. Rubel, V. Lukin, A. Rubel, K. Egiazarian // Remote Sensing. – 2021. – Vol. 13, № 10. – P. 1887. – DOI: https://doi.org/10.3390/rs13101887.
6. Bergstra J. Random search for hyper-parameter optimization / J. Bergstra, Y. Bengio // Journal of Machine Learning Research. – 2012. – Vol. 13. – P. 281–305.
7. Cherepanov I. Research of different methods of threshold selection for the DCT-SSA filter / I. Cherepanov // Herald of Khmelnytskyi National University. Technical Sciences. – 2025. – Vol. 349, № 2. – P. 67–74. – DOI: https://doi.org/10.31891/2307-5732-2026-349-67.
8. Sandler M. MobileNetV2: Inverted residuals and linear bottlenecks / M. Sandler, A. Howard, M. Zhu, A. Zhmoginov, L.-C. Chen // Proceedings of the IEEE Conference on Computer Vision and Pattern Recognition (CVPR). – 2018. – P. 4510–4520. – DOI: https://doi.org/10.1109/CVPR.2018.00474.
9. Bishop C. M. Pattern Recognition and Machine Learning / C. M. Bishop. – New York : Springer, 2006. – 738 p.
10. James G. An Introduction to Statistical Learning: with Applications in R / G. James, D. Witten, T. Hastie, R. Tibshirani. – 2nd ed. – New York : Springer, 2021. – 607 p.
11. Al-Senaikh R. Predicting filtered image quality using transfer learning on Sentinel-1 speckle noise with DenseNet-121 / R. Al-Senaikh, O. Rubel // Ukrainian Journal of Remote Sensing. – 2025. – ISSN: 2313-2132 (Online). – (Submitted).
12. Rubel O. Reduction of Spatially Correlated Speckle in Textured SAR Images / O. Rubel, V. Lukin, S. Krivenko, V. Pavlikov, S. Zhyla, E. Tserne // International Journal of Computing. – 2021. – Vol. 20, № 3. – P. 319–327. – DOI: https://doi.org/10.47839/ijc.20.3.2276.

13. Ieremeiev O. Full-Reference Quality Metric Based on Neural Network to Assess the Visual Quality of Remote Sensing Images / O. Ieremeiev, V. Lukin, K. Okarma, K. Egiazarian // Remote Sensing. – 2020. – Vol. 12, № 15. – P. 2349. – DOI: https://doi.org/10.3390/rs12152349.

14. Lukin V. Saliency map in image visual quality assessment and processing / V. Lukin, E. Bataeva, S. Abramov // Radioelectronic and Computer Systems. – 2023. – № 1. – P. 112–121.

15. Wang Z. Image quality assessment: from error visibility to structural similarity / Z. Wang, A. C. Bovik, H. R. Sheikh, E. P. Simoncelli // IEEE Transactions on Image Processing. – 2004. – Vol. 13, № 4. – P. 600–612. – DOI: https://doi.org/10.1109/TIP.2003.819861.

16. Zhang L. FSIM: A feature similarity index for image quality assessment / L. Zhang, L. Zhang, X. Mou, D. Zhang // IEEE Transactions on Image Processing. – 2011. – Vol. 20, № 8. – P. 2378–2386. – DOI: https://doi.org/10.1109/TIP.2011.2109730.

17. Reisenhofer R. A Haar wavelet-based perceptual similarity index for image quality assessment / R. Reisenhofer, S. Bosse, G. Kutyniok, T. Wiegand // Signal Processing: Image Communication. – 2018. – Vol. 61. – P. 33–43. – DOI: https://doi.org/10.1016/j.image.2017.11.001.

18. Nafchi H. Z. Mean Deviation Similarity Index: Efficient and reliable full-reference image quality evaluator / H. Z. Nafchi, A. Shahkolaei, R. Farrahi-Moghaddam, M. Cheriet // IEEE Access. – 2016. – Vol. 4. – P. 5579–5590. – DOI: https://doi.org/10.1109/ACCESS.2016.2604042.

19. Filipponi F. Sentinel-1 GRD preprocessing workflow / F. Filipponi // Proceedings. – 2019. – Vol. 18, № 11. – DOI: https://doi.org/10.3390/ECRS-3-06201.

References

1. Oliver C. Understanding Synthetic Aperture Radar Images / C. Oliver, S. Quegan. – Raleigh : SciTech Publishing, 2004. – 480 p.

2. Lee J. S. Polarimetric Radar Imaging: From Basics to Applications / J. S. Lee, E. Pottier. – Boca Raton : CRC Press, 2009. – 386 p.

3. Touzi R. A review of speckle filtering in the context of estimation theory / R. Touzi // IEEE Transactions on Geoscience and Remote Sensing. – 2002. – Vol. 40, № 11. – P. 2392–2404. – DOI: https://doi.org/10.1109/TGRS.2002.803727.

4. Lee J. S. Digital image enhancement and noise filtering by use of local statistics / J. S. Lee // IEEE Transactions on Pattern Analysis and Machine Intelligence. – 1980. – Vol. 2, № 2. – P. 165–168. – DOI: https://doi.org/10.1109/TPAMI.1980.4766994.

5. Rubel O. Selection of Lee filter window size based on despeckling efficiency prediction for Sentinel SAR images / O. Rubel, V. Lukin, A. Rubel, K. Egiazarian // Remote Sensing. – 2021. – Vol. 13, № 10. – P. 1887. – DOI: https://doi.org/10.3390/rs13101887.

6. Bergstra J. Random search for hyper-parameter optimization / J. Bergstra, Y. Bengio // Journal of Machine Learning Research. – 2012. – Vol. 13. – P. 281–305.

7. Cherepanov I. Research of different methods of threshold selection for the DCT-SSA filter / I. Cherepanov // Herald of Khmelnytskyi National University. Technical Sciences. – 2025. – Vol. 349, № 2. – P. 67–74. – DOI: https://doi.org/10.31891/2307-5732-2026-349-67.

8. Sandler M. MobileNetV2: Inverted residuals and linear bottlenecks / M. Sandler, A. Howard, M. Zhu, A. Zhmoginov, L.-C. Chen // Proceedings of the IEEE Conference on Computer Vision and Pattern Recognition (CVPR). – 2018. – P. 4510–4520. – DOI: https://doi.org/10.1109/CVPR.2018.00474.

9. Bishop C. M. Pattern Recognition and Machine Learning / C. M. Bishop. – New York : Springer, 2006. – 738 p.

10. James G. An Introduction to Statistical Learning: with Applications in R / G. James, D. Witten, T. Hastie, R. Tibshirani. – 2nd ed. – New York : Springer, 2021. – 607 p.

11. Al-Senaikh R. Predicting filtered image quality using transfer learning on Sentinel-1 speckle noise with DenseNet-121 / R. Al-Senaikh, O. Rubel // Ukrainian Journal of Remote Sensing. – 2025. – ISSN: 2313-2132 (Online). – (Submitted).

12. Rubel O. Reduction of Spatially Correlated Speckle in Textured SAR Images / O. Rubel, V. Lukin, S. Krivenko, V. Pavlikov, S. Zhyla, E. Tserne // International Journal of Computing. – 2021. – Vol. 20, № 3. – P. 319–327. – DOI: https://doi.org/10.47839/ijc.20.3.2276.

13. Ieremeiev O. Full-Reference Quality Metric Based on Neural Network to Assess the Visual Quality of Remote Sensing Images / O. Ieremeiev, V. Lukin, K. Okarma, K. Egiazarian // Remote Sensing. – 2020. – Vol. 12, № 15. – P. 2349. – DOI: https://doi.org/10.3390/rs12152349.

14. Lukin V. Saliency map in image visual quality assessment and processing / V. Lukin, E. Bataeva, S. Abramov // Radioelectronic and Computer Systems. – 2023. – № 1. – P. 112–121.

15. Wang Z. Image quality assessment: from error visibility to structural similarity / Z. Wang, A. C. Bovik, H. R. Sheikh, E. P. Simoncelli // IEEE Transactions on Image Processing. – 2004. – Vol. 13, № 4. – P. 600–612. – DOI: https://doi.org/10.1109/TIP.2003.819861.

16. Zhang L. FSIM: A feature similarity index for image quality assessment / L. Zhang, L. Zhang, X. Mou, D. Zhang // IEEE Transactions on Image Processing. – 2011. – Vol. 20, № 8. – P. 2378–2386. – DOI: https://doi.org/10.1109/TIP.2011.2109730.

17. Reisenhofer R. A Haar wavelet-based perceptual similarity index for image quality assessment / R. Reisenhofer, S. Bosse, G. Kutyniok, T. Wiegand // Signal Processing: Image Communication. – 2018. – Vol. 61. – P. 33–43. – DOI: https://doi.org/10.1016/j.image.2017.11.001.

18. Nafchi H. Z. Mean Deviation Similarity Index: Efficient and reliable full-reference image quality evaluator / H. Z. Nafchi, A. Shahkolaei, R. Farrahi-Moghaddam, M. Cheriet // IEEE Access. – 2016. – Vol. 4. – P. 5579–5590. – DOI: https://doi.org/10.1109/ACCESS.2016.2604042.

19. Filipponi F. Sentinel-1 GRD preprocessing workflow / F. Filipponi // Proceedings. – 2019. – Vol. 18, № 11. – DOI: https://doi.org/10.3390/ECRS-3-06201.